Impact of North Atlantic Sea Surface Temperature Anomaly on Interannual Variability of Summer Atmospheric Heat Source over the Tibetan Plateau

HAIPENG YU,[a] HONGYU LUO,[a,b] JIANPING HUANG,[c] ZEYONG HU,[a] SHANLING CHENG,[a,b] JIE ZHOU,[c] AKINWALE T. OGUNRINDE,[d] HAOJIE WU,[a,b] AND CHENXI LIU[e]

[a] *State Key Laboratory of Cryospheric Science and Frozen Soil Engineering, Nagqu Plateau Climate and Environment Observation and Research Station of Tibet Autonomous Region, Northwest Institute of Eco-Environment and Resources, Chinese Academy of Sciences, Lanzhou, China*

[b] *University of Chinese Academy of Sciences, Beijing, China*

[c] *Key Laboratory of Semi-Arid Climate Change of the Ministry of Education, College of Atmospheric Sciences, Lanzhou University, Lanzhou, China*

[d] *Key Laboratory of Ecological Safety and Sustainable Development in Arid Lands, Northwest Institute of Eco-Environment and Resources, Chinese Academy of Sciences, Lanzhou, China*

[e] *Lanzhou Regional Climate Center, Gansu Meteorological Bureau, Lanzhou, China*

(Manuscript received 21 July 2024, in final form 31 October 2024, accepted 6 January 2025)

ABSTRACT: The summer atmospheric heat source (AHS) over the Tibetan Plateau (TP), modulated by the midlatitude westerlies and Asian summer monsoon, exerts a crucial influence on regional and global atmospheric circulation and climate change. Previous studies have predominantly focused on the impact of low-latitude tropical ocean–atmosphere forcing signals on the summer AHS over the TP. Notably, the North Atlantic (NA) sea surface temperature anomaly (SSTA), as an upstream signal in mid- and high latitudes, can also significantly affect the summer AHS over the TP by stimulating atmospheric teleconnection wave trains, while the mechanisms and contributions remain unclear. This study explores the interannual variation of the summer AHS over the TP and its correlation with concurrent NA SSTA. The results indicate the NA tripole (NAT)-like SSTA pattern contributes about 20% to the interannual variability of the summer AHS over the southeastern TP. Specifically, when the NAT-like SSTA pattern is in a negative phase (meridional positive–negative–positive pattern), it triggers a teleconnection wave train propagating from west to east, culminating in the positive AHS anomaly over the southeastern TP. Further analysis indicates the presence of anomalous vertical ascending motions associated with the wave train over the southeastern TP. When coupled with the convergence belt of water vapor, it is beneficial to the precipitation in this region. The release of condensation latent heat subsequently emerges as a significant contributor to the positive AHS anomaly. Finally, numerical simulation experiments also validate this impact process. This study elucidates the physical mechanism through which NA SSTA affects the interannual variability of the AHS over the TP in summer, providing a scientific basis for climate prediction and disaster management in the region.

KEYWORDS: Complex terrain; North Atlantic Ocean; Sea surface temperature; Summer/warm season; Atmospheric waves; Interannual variability

1. Introduction

The Tibetan Plateau (TP) is located in central Asia and has the highest average elevation and most complex topography in the world. Known as the "roof of the world" and the "third pole of Earth," the uplift of the TP forms a prominent atmospheric heat source (AHS) that towers into the free atmosphere. Its underlying surface directly acts on the midtropospheric atmosphere, significantly affecting and regulating regional and even global atmospheric circulation and climate patterns (Ye and Gao 1979). In summer, the atmosphere over the TP rises strongly driven by its heating effect; while in winter, it sinks significantly due to the longwave radiation cooling throughout the air column. Wu et al. (1997) applied the Ertel potential vorticity theory and thermal adaptation theory to describe this suction–emission effect caused by the TP thermal forcing as the "sensible heat-driven air pump" and revealed its crucial role in the formation and maintenance of the Asian monsoon (Wu et al. 2012, 2018). Additionally, the AHS over the TP can also affect atmospheric teleconnection wave trains. This means that the thermal effects of the TP are not limited to local circulation but can affect weather and climate in the Northern Hemisphere and even globally by regulating hemispheric-scale atmospheric circulation and sea surface currents (Y. Liu et al. 2020; Sun et al. 2021; Yu et al. 2022; Huang et al. 2023; Xie et al. 2023). Therefore, an in-depth study of the AHS over the TP is essential for a better understanding of the physical mechanisms driving global climate change and provides a scientific foundation for developing effective climate change countermeasures.

There are obvious seasonal differences in the AHS over the TP: It acts as a cold source in winter, a weak heat source in spring, and a strong heat source in summer. In winter and spring, sensible heat is the main component; while in summer, the condensation latent heat released by precipitation (Pre) becomes dominant (Ye and Gao 1979). Due to the strong condensation latent heat, the TP becomes a powerful AHS in the midtroposphere of the Northern Hemisphere during summer. Coupled with the Asian summer monsoon period, the summer AHS over the TP plays a crucial role in the

Corresponding author: Jianping Huang, hjp@lzu.edu.cn

DOI: 10.1175/JCLI-D-24-0404.1

formation and evolution of atmospheric circulation in Asia and the Northern Hemisphere. On account of the significant impact of the summer TP thermal forcing on global climate change, the variability mechanisms of the summer AHS over the TP have gained increasing attention in recent years. The TP is simultaneously influenced by two circulation systems: the midlatitude westerlies and the Asian summer monsoon during summer (Yang et al. 2014; Dong et al. 2017; Zhou et al. 2019; Lai et al. 2021; Wang et al. 2022). This means that the summer AHS over the TP is affected by various ocean–atmosphere forcing signals from both mid–high latitudes and tropical regions. Some studies have shown that the Indian Ocean warm sea surface temperature anomaly (SSTA) can induce Ekman divergence by triggering Kelvin waves, forming an anomalous anticyclone over the Bay of Bengal. This anomalous anticyclone transports water vapor to the southeastern TP via anomalous southwesterlies, leading to a positive precipitation anomaly and the release of condensation latent heat, further affecting the summer AHS over the TP (Hu and Duan 2015; Sun and Wang 2019; Zhao and Zhou 2021; Zhang et al. 2022). Additionally, El Niño–Southern Oscillation (ENSO), as the strongest signal of interannual variability, can significantly affect the summer AHS over the TP due to its close connection with the Indian summer monsoon. During the summer of El Niño development years, the Indian summer monsoon weakens, and an anomalous cyclonic circulation appears in the upper troposphere over the western TP. This inhibits water vapor transport to the western TP, resulting in a negative precipitation anomaly in the region and further affecting the summer AHS over the TP (Wang and Ma 2018; S. Liu et al. 2020; Hu et al. 2021). Through a review of previous studies, we find that the studies available on the anomalous causes of the summer AHS over the TP mostly focus on low-latitude tropical regions, while the research on the forcing signals in mid- and high latitudes still needs to be further investigated.

Many studies have indicated that anomaly in the AHS over the TP results from both atmospheric circulation and external oceanic forcing (Jiang et al. 2016; Wang and Xu 2018; Zhao et al. 2018; Han et al. 2021). The North Atlantic (NA), positioned upstream of the Eurasian continent, with its SSTA, as a signal in mid- and high latitudes, can affect the TP thermal conditions by stimulating atmospheric teleconnection wave trains. Cui et al. (2015) observed that the NA tripole (NAT) SSTA pattern in early spring could alter the strength of the spring subtropical westerly jet over the TP by triggering stationary downstream Rossby waves, further affecting the spring AHS over the TP. Han et al. (2022) found that the horseshoe-like SSTA pattern over the midlatitude NA in October and its persistence in November may be key factors in the precipitation and snow cover anomalies over the central TP. Additionally, some scholars have demonstrated that the quasi-stationary downstream Rossby wave train triggered by the NAT SSTA pattern during winter and spring leads to anomalous cyclonic circulation in the mid- to upper troposphere over the western TP. This circulation transports water vapor from the Arabian Sea to the southwestern TP, resulting in a positive precipitation anomaly and a negative surface sensible heat anomaly in this region (Yu et al. 2021, 2023). In summary, the NA SSTA plays an indispensable role in the anomalous variations of the AHS over the TP. However, current research on the impact of NA SSTA on the AHS over the TP is mostly concentrated on the winter and spring seasons, while the studies on the influence of NA SSTA on the AHS over the TP in summer are still relatively scarce, and the potential physical mechanisms and contributions are not fully understood. Therefore, this article explores the relationship between the summer AHS over the TP and simultaneous NA SSTA on the interannual scale, which is crucial for climate prediction and disaster management in the plateau area.

The remainder of this article is organized as follows: section 2 briefly introduces the data, methods, and model applied in this study; section 3 analyzes the interannual variability of the summer AHS over the TP and its associated atmospheric circulation, explores its correlation with the concurrent NA SSTA and the relevant physical mechanisms, and validates our findings through numerical experiments; and finally, the summary and discussions are provided in section 4.

2. Data, methods, and model

a. Data

The data used in this study include the following: 1) The monthly Japanese 55-year Reanalysis (JRA-55) datasets provided by the Japan Meteorological Agency (JMA) with a horizontal resolution of 1.25° × 1.25° (Kobayashi et al. 2015); 2) the monthly reanalysis datasets from the National Centers for Environmental Prediction–National Center for Atmospheric Research (NCEP/NCAR) with a horizontal resolution of 2.5° × 2.5° for investigating the dynamic mechanism of the wave train (Kalnay et al. 1996); 3) the monthly mean sea surface temperature (SST) data from the National Oceanic and Atmospheric Administration (NOAA) Extended Reconstructed SST, version 5 (ERSST.v5), with a horizontal resolution of 2.0° × 2.0° (Huang et al. 2017); 4) the monthly mean precipitation data provided by the Climatic Research Unit (CRU TS4.06) with a horizontal resolution of 0.5° × 0.5° (Harris et al. 2020); and 5) the datasets of TP boundary provided by the National Tibetan Plateau/Third Pole Environment Data Center (Zhang et al. 2014). The study period spans from 1981 to 2020, with the summer defined as the average from June to August.

b. Methods

1) Atmospheric heat source

The AHS is defined as the gain or loss of heat in the air column, which comprises the sum of sensible heat (SH), condensation latent heat (LH) released to the atmosphere by precipitation, and net radiation of the air column (RC) (Ye and Gao 1979; Yu et al. 2011). The formula is

$$\begin{aligned}\mathrm{AHS} &= \mathrm{SH} + \mathrm{LH} + \mathrm{RC}\\ &= \frac{C_p}{g}\int_{P_t}^{P_s}[(\mathrm{vdfhr} + \mathrm{lrghr} + \mathrm{cnvhr} + \mathrm{lwhr} + \mathrm{swhr})]dp,\end{aligned} \tag{1}$$

where SH represents the vertical integration of the vertical diffusion heating rate (vdfhr), LH is the vertical integration of the large-scale condensation heating rate (lrghr) and the convective heating rate (cnvhr), and RC is the vertical integration of the solar radiative heating rate (swhr) and the longwave radiative heating rate (lwhr). And C_p is the specific heat of dry air at constant pressure, g is the acceleration of the gravity, P_s refers to the surface pressure, and $P_t = 100$ hPa.

2) TAKAYA AND NAKAMURA WAVE ACTIVITY FLUX

The propagation of the wave energy is characterized by the wave activity flux (WAF) (Takaya and Nakamura 2001), and the horizontal WAF is calculated as follows:

$$\mathrm{WAF} = \frac{p\cos\varphi}{2|\mathbf{U}|}\begin{cases}\dfrac{\overline{u}}{a^2\cos^2\varphi}(\psi_x'^2 - \psi'\psi_{xx}') + \dfrac{\overline{v}}{a^2\cos^2\varphi}(\psi_x'\psi_y' - \psi'\psi_{xy}') \\ \dfrac{\overline{u}}{a^2\cos^2\varphi}(\psi_x'\psi_y' - \psi'\psi_{xy}') + \dfrac{\overline{v}}{a^2}(\psi_y'^2 - \psi'\psi_{yy}')\end{cases}, \tag{2}$$

where u and v represent the zonal and meridional wind of the basic flow vector $\mathbf{U}$ (u, v), respectively; p is the pressure; φ is the latitude; $|\mathbf{U}|$ is the wind speed; a is the radius of Earth; ψ is the streamfunction; x and y are the partial derivatives of ψ in the zonal and meridional directions; and "–" and "′" are the climatology and deviation, respectively.

3) LINEARIZED VORTICITY EQUATION

Under the geostrophic approximation, the linearized vorticity equation can be expressed as (Kosaka and Nakamura 2006)

$$\mathrm{RWS} - \underbrace{\overline{u}_\psi\frac{\partial\zeta'}{\partial x}}_{\mathrm{ZA}} - \underbrace{\overline{v}_\psi\frac{\partial\zeta'}{\partial y}}_{\mathrm{MA}} - \underbrace{u_\psi'\frac{\partial\zeta'}{\partial x}}_{\beta\_x} - \underbrace{v_\psi'\frac{\partial(f+\overline{\zeta})}{\partial y}}_{\beta\_y} - \mathrm{Res} = 0, \tag{3}$$

where the RWS is the linearized Rossby wave source; ZA (MA) represents the transport of perturbed vorticity by the zonal (meridional) component of the climatological rotating wind; β_x (β_y) indicates the transport of mean vorticity by the zonal (meridional) component of the perturbed rotating wind; and Res represents the residuals, including the dissipation, nonlinear effects, skew terms, and data uncertainty. The RWS term can also be divided into the vorticity stretching term (related to the convergence and divergence of the flow) and the vorticity advection term (representing the vorticity advection by the divergent wind) (Sardeshmukh and Hoskins 1988), expressed as

$$\mathrm{RWS} = -\nabla_H\cdot\{\mathbf{u}'_\chi(f+\overline{\zeta})\} - \nabla_H\cdot\{\overline{\mathbf{u}}_\chi\zeta'\}, \tag{4}$$

where ∇_H is the horizontal gradient operator, $\mathbf{u} = (u, v)$ refers to the horizontal wind, f represents the Coriolis parameter, and ζ is the relative vorticity. The subscripts χ and ψ represent the divergent and rotational wind component of $\mathbf{u}$, respectively.

4) BAROTROPIC AND BAROCLINIC ENERGY CONVERSION

The barotropic energy conversion (CK) and baroclinic energy conversion (CP) formulated by Kosaka and Nakamura (2006) are calculated as follows:

$$\mathrm{CK} = \frac{v'^2 - u'^2}{2}\left(\frac{\partial\overline{u}}{\partial x} - \frac{\partial\overline{v}}{\partial y}\right) - u'v'\left(\frac{\partial\overline{u}}{\partial y} + \frac{\partial\overline{v}}{\partial x}\right), \tag{5}$$

$$\mathrm{CP} = -\frac{f}{\sigma}\left(v'T'\frac{\partial\overline{u}}{\partial p} - u'T'\frac{\partial\overline{v}}{\partial p}\right), \tag{6}$$

where $\sigma = (R\overline{T}/C_p p) - (d\overline{T}/dp)$ is the atmospheric stability parameter. The R and C_p denote the gas constant and specific heat at constant pressure, respectively.

c. *Model*

Sensitivity experiments were conducted using the Community Atmospheric Model, version 6.0 (CAM6) (Danabasoglu et al. 2020), of the Community Earth System Model (CESM) developed by the NCAR to examine whether the NA SSTA can excite a wave train propagating downstream to the TP and affect the AHS over the TP during summer. This mode utilizes the finite-volume dynamical core (Lin and Rood 1997) and incorporates enhanced physical parameterizations compared to previous versions. It operates at a horizontal resolution of 0.9° (in latitude) × 1.25° (in longitude), with 32 vertical levels, and a model top at 2.26 hPa.

3. Results

a. *Interannual variability of the summer AHS over the TP and associated anomalous circulation*

In this section, we examine the interannual variability of the summer AHS over the TP and the distribution of associated anomalous circulation during the period from 1981 to 2020. To emphasize the interannual variability, we detrend the linear trend of the data and conduct the filtering techniques (subtracting the 9-yr running average from the original data) to isolate interannual signals. Figure 1a illustrates the spatial distribution of the climatological state and interannual standard deviation of the summer AHS over the TP. During summer, the entire TP acts as a heat source, with peaks concentrated in the southeastern TP, reaching up to 200 W m^{-2}. This is primarily due to the release of condensation latent heat from summer precipitation (Luo et al. 2024). The interannual standard deviation of the

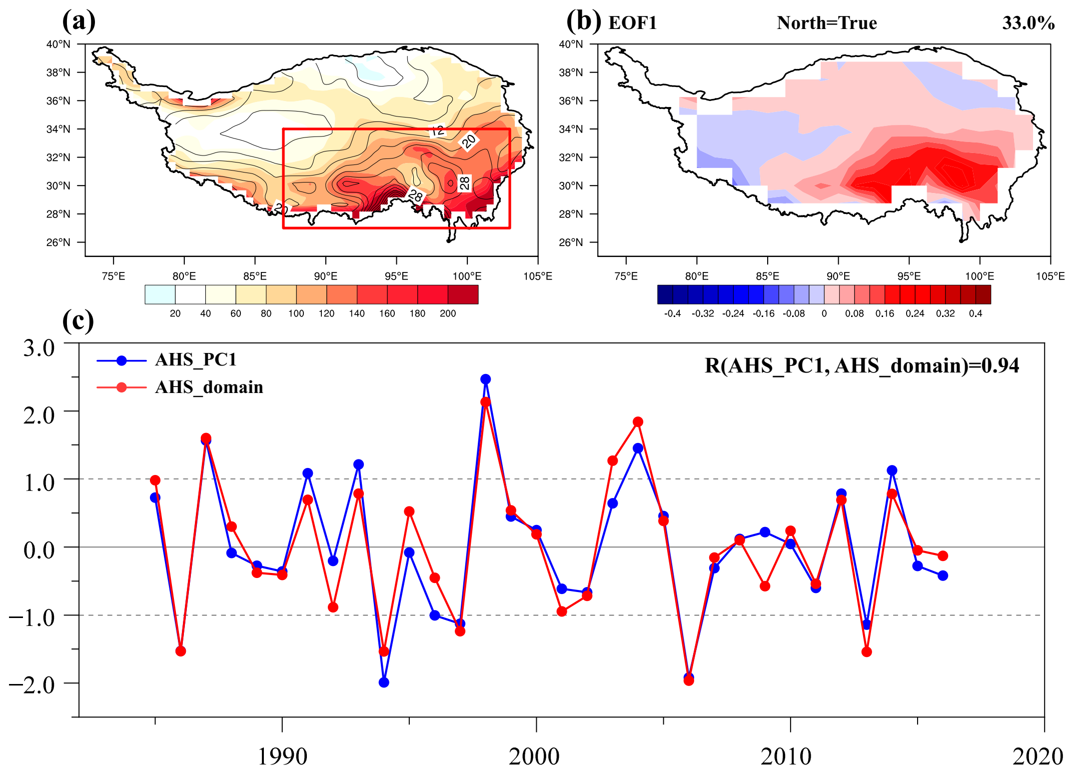

FIG. 1. (a) Spatial distribution of the summer AHS over the TP (W m^{-2}; shading) and standard deviation of its interannual variations (W m^{-2}; black contour) during 1981–2020. The red rectangle box (87°–103°E, 27°–34°N) denotes the key region. (b) Spatial pattern of the EOF1 of the summer AHS over the TP during 1981–2020. The percentage in the top right is the percent variance explained by the EOF1. (c) Normalized AHS index obtained by the area-weighted average over the key region (AHS_domain, red line) and the normalized PC corresponding to the EOF1 (AHS_PC1, blue line). The number in the top right is the correlation coefficient between AHS_domain and AHS_domain.

summer AHS also exhibits high values in the southeastern TP, indicating significant interannual variability in this region. Consequently, we identify the southeastern TP (87°–103°E, 27°–34°N) as the key region for analyzing the interannual variability of the summer AHS over the TP. Additionally, we present the spatial distribution of the first leading mode for the empirical orthogonal function (EOF1) of the interannual variability of the summer AHS over the TP in Fig. 1b. The EOF1 accounts for 33.0% of the total variance and passes the North test. The primary anomaly center of the summer AHS is also situated in the southeastern TP, while a smaller area in the western and northeastern TP displays a reverse-phase pattern, though with weaker intensity. We perform an area-weighted average and standardization on the interannual series of the summer AHS over the key region in the southeastern TP (highlighted by the red rectangle box in Fig. 1a) to establish the AHS index. The temporal correlation coefficient between this index (AHS_domain, indicated by the red line in Fig. 1c) and the normalized principal component (PC) corresponding to EOF1 (AHS_PC1, represented by the blue line in Fig. 1c) is 0.94, statistically significant at the 99% confidence level. Thus, the index AHS_domain effectively captures the interannual variation of the summer AHS over the TP.

Figure 2 illustrates the spatial distributions of the summer 200-hPa meridional wind, 200-hPa geopotential height, and horizontal WAF, as well as the 500-hPa geopotential height and wind field anomalies regressed to the AHS_domain. As can be seen in Fig. 2a, there is a teleconnection wave train propagating from west to east from the NA in mid- and high latitudes of Eurasia. The wave train appears to result from the coupled relation between the waveguide teleconnections along the polar front jet and along the subtropical jet, as examined by Xu et al. (2022). It bifurcates near the Caspian Sea, with the northern branch continuing to propagate eastward along the polar front jet in the upper troposphere as far as the Sea of Okhotsk region, and the other branch propagating south-eastward along the subtropical westerly jet to East Asia. Among them, the activity centers of the northern branch of the wave train are basically consistent with those of the British–Baikal Corridor (BBC) teleconnection pattern (Xu et al. 2019); and the activity centers of the southern branch of the wave train are distributed on the east and west sides of the TP. The anomalous WAF distinctly shows the propagation path of Rossby wave energy. As depicted by the 200-hPa horizontal WAF (Fig. 2b), this wave train originates from the western NA, corresponding to the exit zone of the

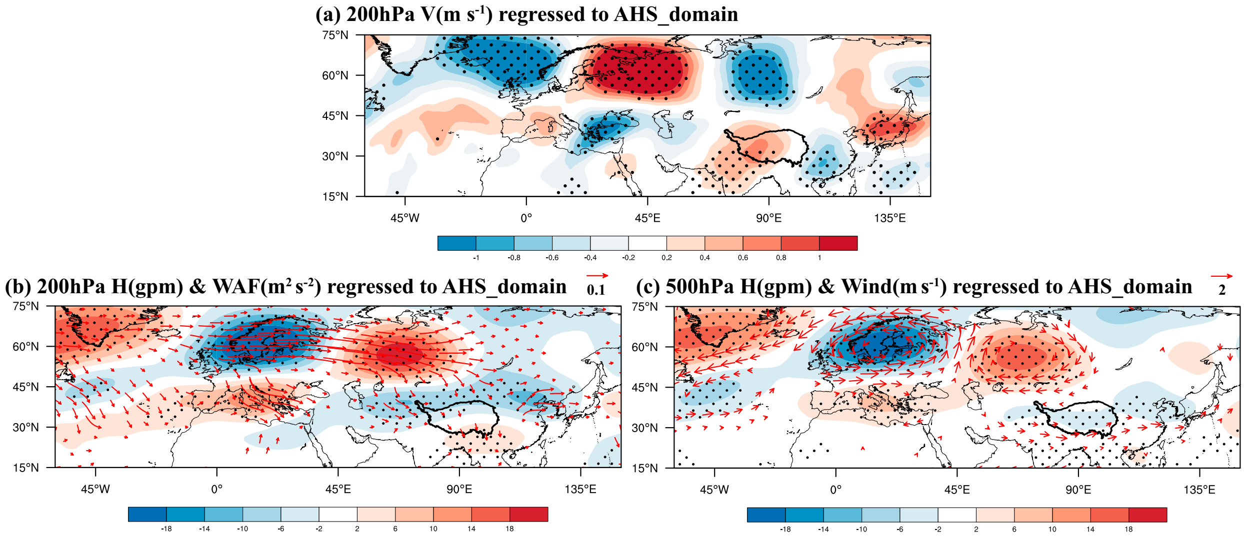

FIG. 2. The summer (a) 200-hPa meridional wind (V, m s^{-1}; shading), (b) 200-hPa geopotential height (H, gpm; shading) and WAF (m^2 s^{-2}; vector), and (c) 500-hPa geopotential height (H, gpm; shading) and wind (m s^{-1}; vector) anomalies regressed to the AHS_domain. The dotted areas are significant at the 90% confidence level. Only wind anomalies statistically significant at the 0.1 level are plotted.

NA jet, effectively exciting disturbances. The wave train undergoes disturbances, generating low-frequency oscillations that influence the weather and climate of downstream regions through energy propagation and dispersion effects. When the summer AHS over the TP is anomalously strong, the wave train extends from the NA across western Europe, central Asia, and the Iranian Plateau to the southeastern TP. The geopotential height anomalies over these regions exhibit a pattern of "+, −, +, −, +," with most areas significant at the 90% confidence level. The positive geopotential height anomaly over the southeastern TP corresponds to the intensified South Asian high induced by the abnormally strong summer AHS over the TP. Furthermore, the comparison of the 200- and 500-hPa geopotential height anomalies (Figs. 2b,c) reveals a similar spatial structure of the wave train, characterized by "weaker in the lower levels and stronger in the upper levels," indicating an equivalent barotropic structure in the vertical direction of the atmospheric circulation associated with the interannual variation of the summer AHS over the TP.

b. Relationship between the NA SSTA and the AHS over the TP in summer

Upon analyzing the large-scale circulation associated with the interannual variations of the summer AHS over the TP in the preceding section, it becomes evident that the external forcing signals affecting the interannual variability of the summer AHS over the TP may originate from the western NA. Consequently, singular value decomposition (SVD) analysis was conducted to examine the relationship between the interannual variations of the summer AHS over the TP and the concurrent NA SSTA. The AHS over the TP was designated as the left field and the NA SST as the right field. Similarly, before conducting the SVD analysis, the AHS and SST data were detrended and filtered. Figure 3 presents the heterogeneous correlation spatial distributions and the normalized time series of the first leading SVD mode (SVD1) of these two fields. SVD1 accounts for 52.33% of the total explained variance, with a temporal correlation coefficient of 0.71 between the time series of the left and the right fields, significant at the 99% confidence level. This indicates a close relationship between the interannual variability of the AHS over the TP and the NA SSTA in summer. SVD1 of the AHS over the TP (Fig. 3a) exhibits a similar spatial distribution to its EOF1 (Fig. 1b), with the high-value area situated in the southeastern TP. The correlation coefficient between AHS_SVD1 and AHS_domain is 0.95, significant at the 99% confidence level. The SVD1 of NA SST (Fig. 3b) displays a "+, −, +" mode from south to north, similar to the NAT pattern. By comparison, we find that compared with the NAT pattern, the maximum centers of SST_SVD1 shift slightly to the east and south (Cheng et al. 2024). In addition, we calculate the correlation coefficient between SST_SVD1 and NAT to be 0.69. Therefore, we define the SST_SVD1 as the NAT-like SSTA pattern. In line with the definition by previous studies (Wu et al. 2009; Zuo et al. 2013), the spatial mode shown in Fig. 3b can be referred to as the negative phase pattern of NAT-like SSTA, and the opposite is called the positive phase pattern. The results of SVD1 indicate that when the negative phase pattern of NAT-like SSTA predominates, the summer AHS over the TP strengthens anomalously.

Based on the findings of SVD, the SST_SVD1 in Fig. 3c was designated as the NAT-like SSTA index series correlated with the interannual variability of the summer AHS over the TP in this current study. Subsequently, the 200-hPa meridional wind, 200-hPa geopotential height, and horizontal WAF, as well as the 500-hPa geopotential height and wind field anomalies, were regressed against the SST_SVD1 (Figs. 4a,b,d). The regression results reveal a distinct wave train structure in the upper troposphere propagating from the western NA to the Eurasian

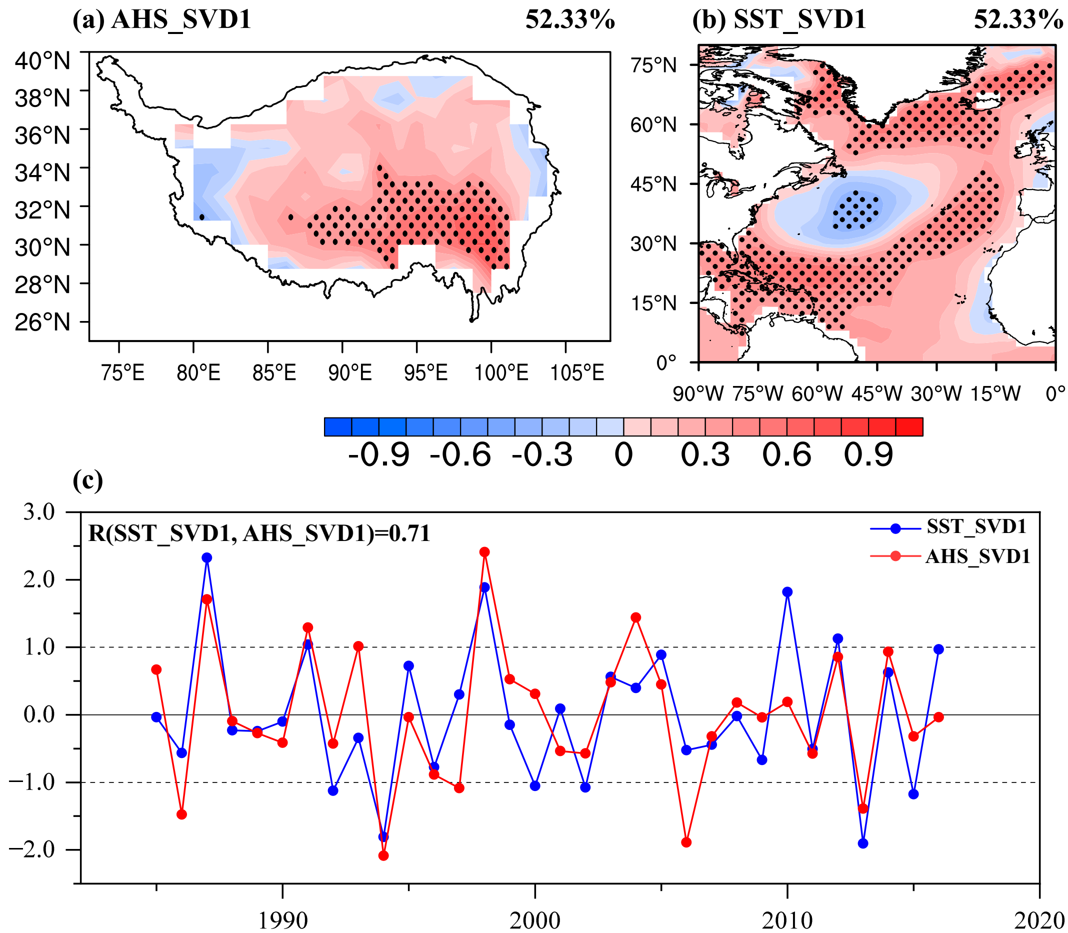

FIG. 3. Heterogeneous correlation patterns of the summer (a) AHS over the TP and (b) NA SST for the SVD1 during 1981–2020. The dotted areas are significant at the 90% confidence level, and the values in the top right are the percentages of explained variance. (c) Normalized expansion coefficients of the SVD1 for the summer AHS over the TP (AHS_SVD1, red line) and NA SST (SST_SVD1, blue line).

continent, extending to the southeastern TP. These spatial distributions align with those depicted in Fig. 2, suggesting a significant contribution of the NAT-like SSTA pattern to the interannual variability of the AHS over the TP in summer. By following the propagation path of the wave train triggered by NA SSTA, Fig. 4c provides the vertical cross section of temperature, geopotential height, and vertical velocity anomalies along the thick solid lines labeled A, B, C, D, and E (marked in Fig. 4b) regressed to SST_SVD1. Consistent with earlier analyses, the anomalous temperature and geopotential height fields manifest a clear wave train structure propagating from west to east. The geopotential height of the A-D section demonstrates an equivalent barotropic structure vertically, with the maximum center of anomaly positioned around 250 hPa. While the temperature field over the TP slightly lags behind the height field in phase, it exhibits a baroclinic structure with a westward tilt from bottom to top in the mid- and lower troposphere due to the powerful diabatic heating (Fang and Yang 2016). Owing to the baroclinic nature of the atmosphere, which leads to the development of trough and ridge systems. And from Fig. 4c, significant anomalous upward motions are observed over the TP. This is conducive to the development of convection, leading to increased precipitation and the release of condensation latent heat in the region, thereby intensifying the summer AHS over the TP. According to the thermal adaptation theory, the positive AHS anomaly over the TP can also induce the baroclinic structure of a lower-level cyclone and an upper-level anticyclone. Thus, there exist positive feedback between this baroclinic structure and the positive AHS anomaly over the TP, favoring the enhancement of each other, and thus strengthening the response of AHS and circulation over the TP to the NAT-like SSTA pattern forcing. In addition, we can see from Fig. 3b that there are three centers for the NAT-like SSTA pattern, and it seems that the two warm SST centers are stronger and larger than the cold SST in the middle center. We performed a partial regression analysis to distinguish the effects of the three centers and used the standard regression coefficients to explain their relative contributions (not shown). The results show that the cold SST center has a weak negative contribution to the AHS

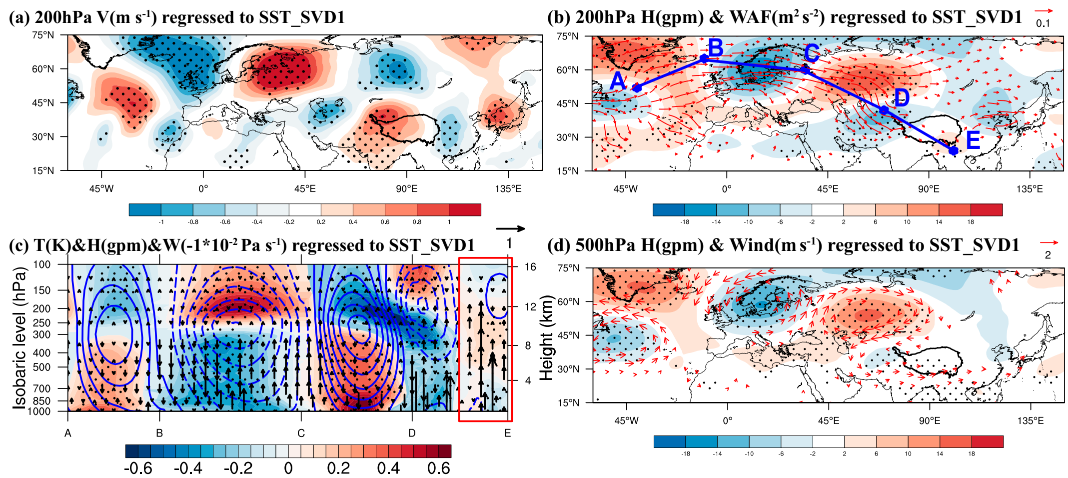

FIG. 4. The summer (a) 200-hPa meridional wind (V, m s^{-1}; shading); (b) 200-hPa geopotential height (H, gpm; shading) and WAF (m^2 s^{-2}; vector); (c) vertical cross section of the temperature (T, K; shading), geopotential height (H, gpm; contour), and vertical velocity (W, -1×10^{-2} Pa s^{-1}; vector) along the thick solid lines labeled A, B, C, D, and E in (b); and (d) 500-hPa geopotential height (H, gpm; shading) and wind (m s^{-1}; vector) anomalies regressed to the SST_SVD1. The dotted areas are significant at the 90% confidence level. Only wind anomalies statistically significant at the 0.1 level are plotted.

anomalies over the TP, while the two warm SST centers have strong positive contributions.

c. *The dynamic mechanism of the wave train*

The preceding analysis indicates that the summer NAT-like SSTA pattern triggers an atmospheric teleconnection wave train that propagates downstream along the great circle path, affecting the circulation systems over the TP. In this section, we analyze the dynamical mechanisms of generation and maintenance of this wave train, which is of great significance for understanding its spatial structure. Figure 5 presents the budget of various terms in the linearized vorticity equation corresponding to the wave train. The figure shows that the RWS, ZA, and β_y are the dominant terms in the vorticity equation. In contrast, the MA and β_x contribute minimally to the wave train. Specifically, the RWS (Fig. 5a) comprises alternating centers of positive and negative sources along the path shown in Fig. 4b, with a distinct negative anomaly center in the western NA. The distribution of RWS at high latitude is similar to that of the BBC teleconnection pattern (Xu et al. 2019), corresponding to the analysis about Fig. 2a. We further decompose the RWS term (Sardeshmukh and Hoskins 1988), and the comparison shows that the RWS is predominantly contributed by the vorticity stretching term (Fig. 6a), indicating that the generation of RWS is mainly related to convergence and divergence in the upper troposphere. Meanwhile, the spatial configuration of the ZA is located downstream of the wave train (Fig. 5b), originating from the downstream zonal advection of perturbed vorticity by the climatological rotating wind. Additionally, the ZA (Fig. 5b) and β_y (Fig. 5e) are nearly compensatory in their spatial distribution and magnitude, suggesting that the zonal advection of perturbed vorticity by the climatological rotating wind can be offset by the meridional advection of mean vorticity by the perturbed rotating wind. As for the Res term (Fig. 5f), which represents dissipation, nonlinear effect, skew term, and data uncertainty, no further investigation was conducted. This is due to its smaller magnitude compared to the RWS and ZA terms, as well as the absence of a systematic spatial structure.

The discussion above focused on the vorticity budget, and the subsequent analysis will explore the maintenance mechanism of the wave train from the perspective of energetics. Figure 7 shows the vertical integration (from 1000 to 100 hPa) of CK and CP between the wave train and the mean flow. As seen in Fig. 7a, the CK is primarily concentrated near the exit region of the NA jet and the Asian jet, indicating the energy conversion of perturbed kinetic energy between the basic flow and the wave train in these areas, although the overall intensity is relatively weak. In comparison, the contribution of CP is greater than that of CK, exhibiting alternating positive and negative values along the wave train (Fig. 7b), which is consistent with the structure of the wave train shown in Fig. 4b. The predominance of positive over negative values suggests that the wave train can effectively extract available potential energy from the mean flow and is sustained through the process of baroclinic energy conversion. Therefore, CP plays a major role in maintaining the wave train, while CK has a relatively limited effect and mainly serves to fix the position of the wave train.

d. *Impact of the NAT-like SSTA pattern on summer AHS over the TP*

The generation and maintenance mechanisms of the teleconnection wave train excited by the summer NAT-like SSTA pattern from the perspective of atmospheric internal dynamics were discussed in the preceding section. Subsequently, an examination of the physical processes through which this wave train affects the summer AHS over the TP will be undertaken. Figure 8

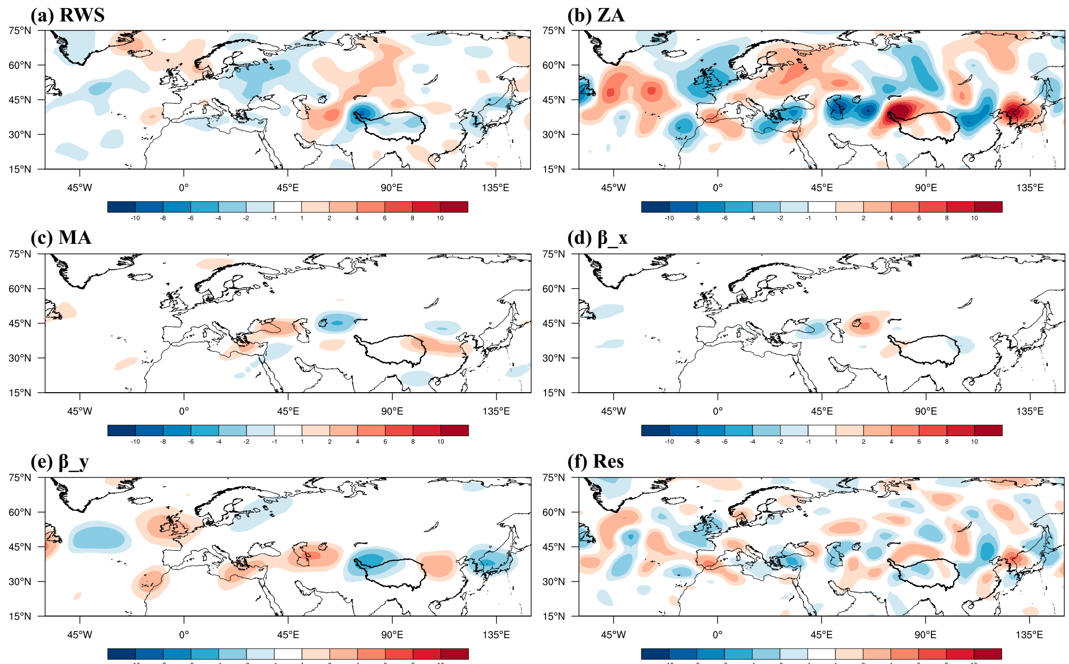

FIG. 5. The summer vorticity budget of the Rossby wave train at 200-hPa (10^{-11} s^{-2}; shading) anomalies regressed to the SST_SVD1. (a) RWS, (b) transport of perturbed vorticity by the zonal component of the climatological rotating wind (ZA), (c) transport of perturbed vorticity by the meridional component of the climatological rotating wind (MA), (d) transport of mean vorticity by the zonal component of the perturbed rotating wind (β_x), (e) transport of mean vorticity by the meridional component of the perturbed rotating wind (β_y), and (f) Res.

displays the anomalous horizontal and vertical spatial patterns of the summer AHS over the TP and its three components regressed to the SST_SVD1. The Fig. 8a indicates a significant positive AHS anomaly over the southeastern TP, closely resembling the spatial distribution of AHS_SVD1 depicted in Fig. 3a. When the NAT-like SSTA pattern is in the negative phase, the AHS is abnormally strong across most TP regions. As for the AHS components, the spatial distribution of condensation latent heat closely corresponds to that of the AHS, with a large magnitude (Fig. 8b). This indicates the predominant influence of condensation latent heat released by precipitation on the summer AHS anomaly over the TP. In contrast, the spatial distribution of sensible heat opposes to that of the AHS and condensation latent heat, with a smaller magnitude but significant over the southeastern TP (Fig. 8c). The atmospheric net radiation displays a negative anomaly across the majority of the TP, exhibiting the smallest magnitude and generally insignificant variations throughout the region (Fig. 8d). Furthermore, analysis of the vertical distributions of the summer AHS and its components (Fig. 8e) reveals a strong positive anomaly of the summer AHS below 250 hPa, primarily driven by condensation latent heat. The condensation latent heat exhibits a positive anomaly throughout the layer, with significant values concentrated in the midtroposphere, closely aligning with cloud height distribution over the TP in summer. Sensible heat displays a notable negative anomaly primarily in the near-surface layer of the TP, constrained by vertical transport limitations. In terms of atmospheric net radiation, a heating effect is observed below 500 hPa in the near-surface layer due to the absorption of longwave radiation emitted from the surface. While above 500 hPa up to the tropopause, longwave radiation cooling, primarily influenced by cloud layers, plays a key role. The heating effect of shortwave

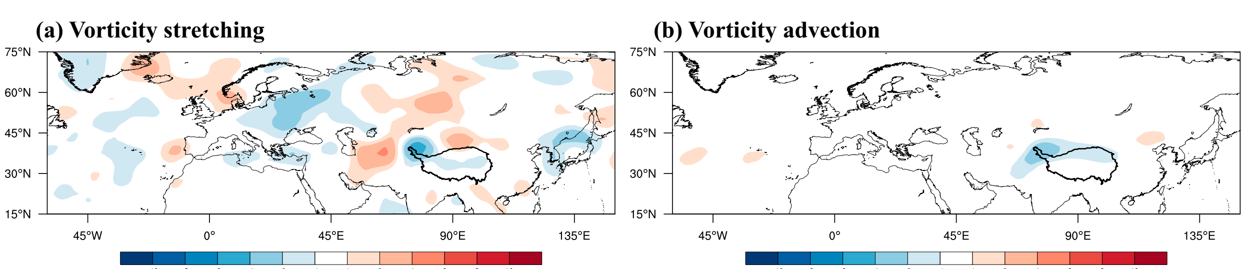

FIG. 6. The summer (a) vorticity stretching term and (b) vorticity advection term of the RWS (10^{-11} s^{-2}; shading) anomalies regressed to the SST_SVD1.

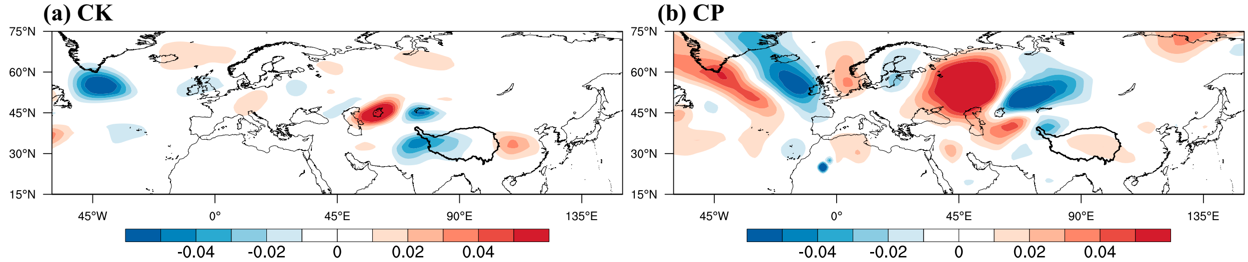

FIG. 7. The summer vertically integrated (a) CK and (b) CP (W m^{-2}; shading) anomalies regressed to the SST_SVD1.

radiation caused by clouds and aerosols is comparatively weaker. Following the offsetting of these opposing influences, the atmospheric net radiation indicates a heating effect below 400 hPa and a cooling effect above 400 hPa, resulting in insignificant changes after vertical integration of the entire layer (Fig. 8d).

Furthermore, an analysis is conducted on the factors linked to the three components of the AHS. Initially, for the condensation latent heat, the anomalous spatial patterns of the 500-hPa vertical velocity (W), total cloud cover (TCC), vertically integrated water vapor flux (Qflux) and water vapor divergence (Qflux_div), and precipitation (Pre) over the TP regressed against SST_SVD1 are illustrated in Figs. 9a–d, with peak values consistently situated in the southeastern TP. When the NAT-like SSTA is in the negative phase, anomalous upward motions appear over the southeastern TP (in agreement with prior profile analyses), promoting convective development and leading to an increase in total cloud cover. Simultaneously, a convergence zone of water vapor forms over the southeastern TP, transporting more water vapor from the tropical ocean to this region, favoring precipitation and thereby enhancing the condensation latent heat. Second, regarding the sensible heat, previous research has shown that its anomalous variations predominantly depend on the ground-air temperature difference ($T_s - T_a$, where T_s is the ground temperature and T_a is the air temperature) and the 10-m wind speed (10 m V) (Yang et al. 2009). Figures 9e and 9f depict the anomalous spatial patterns of $T_s - T_a$ and 10 m V over the TP regressed against SST_SVD1. The comparison reveals that the negative sensible heat anomaly (Fig. 8b) is predominantly caused by the negative $T_s - T_a$ anomaly (Fig. 9e), with both anomalies exhibiting a similar spatial distribution, particularly peaking over the southeastern TP. The increased precipitation over the southeastern TP leads to decreased Ts, subsequently reducing $T_s - T_a$. Conversely, in the western and northern TP, sparse vegetation and exposed surfaces allow solar radiation to reach the ground directly, coupled with reduced precipitation, rapidly increasing T_s thereby enlarging $T_s - T_a$. However, the 10-m V shows an opposite variation to sensible heat, displaying a positive anomaly across most of the TP, with the peak values centered over the southwestern TP (Fig. 9f), partly offsetting the negative contribution of $T_s - T_a$ to sensible heat. Subsequently, with regard to atmospheric net radiation, Figs. 9g–l illustrate the regression fields of net longwave flux, net shortwave flux, and associated radiation components against SST_SVD1. The increase in total cloud cover over the southeastern TP results in greater absorption of shortwave flux by the atmosphere, hence boosting the net shortwave flux (Fig. 9h). Concurrently, more shortwave flux is reflected back to space (Fig. 9i), reducing the solar radiation reaching the surface (Fig. 9j). Moreover, in combination with the cooling impact of precipitation on

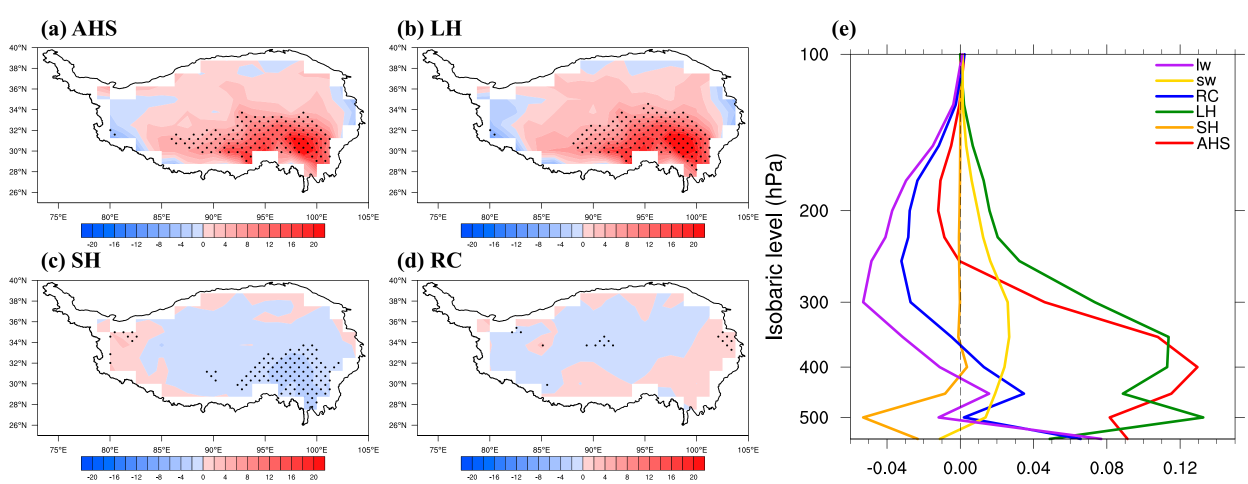

FIG. 8. The summer (a) AHS, (b) LH, (c) SH, (d) RC (W m^{-2}; shading), and (e) diabatic heating profiles (K day^{-1}; line) anomalies over the TP regressed to the SST_SVD1. The red, orange, green, blue, yellow, and purple lines represent the AHS, SH, LH, RC, net shortwave radiative (sw), and net longwave radiative (lw), respectively. The dotted areas are significant at the 90% confidence level.

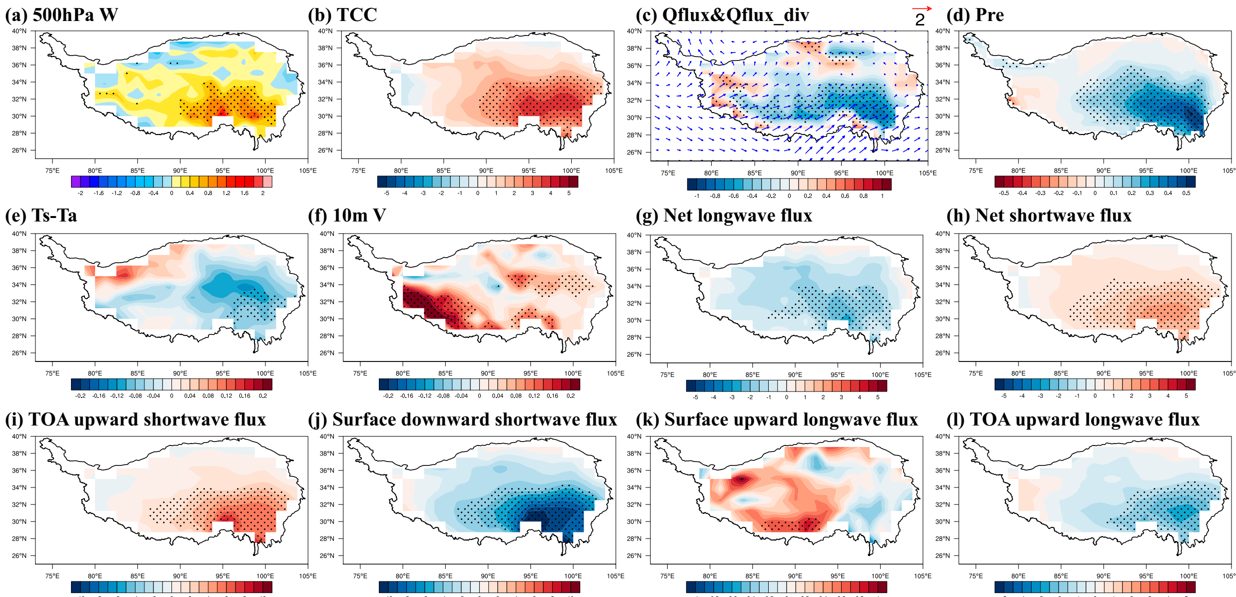

FIG. 9. The summer (a) 500-hPa W (-1×10^{-2} Pa s^{-1}; shading), (b) TCC (%; shading), (c) Qflux (kg m^{-1} s^{-1}; shading) and Qflux_div (kg m^{-2} s^{-1}; vector), (d) Pre (mm day^{-1}; shading), (e) *T_s* − *T_a* (K; shading), (f) 10-m V (m s^{-1}; shading), (g) net longwave flux (W m^{-2}; shading), (h) net shortwave flux (W m^{-2}; shading), (i) upward shortwave flux at the TOA anomalies (W m^{-2}; shading), (j) downward shortwave flux at the surface (W m^{-2}; shading), (k) upward longwave flux at the surface (W m^{-2}; shading), and (l) upward longwave flux at the TOA (W m^{-2}; shading) over the TP regressed to the SST_SVD1. The dotted areas are significant at the 90% confidence level.

the surface, T_s diminishes, emitting less longwave flux upward from the surface (Fig. 9k). Additionally, the abundant total cloud cover over the southeastern TP results in a dense atmosphere with low cloud-top temperatures, further reducing the outgoing longwave flux at the top of the atmosphere (Fig. 9l). From a perspective on net balance, the entire atmospheric column exhibits a cooling effect (Fig. 9g). The offsetting of the cooling of net longwave flux and the heating of net shortwave flux, both in terms of spatial distribution and magnitude, results in a relatively minor fluctuation in overall atmospheric net radiation, aligning with the analysis presented in Fig. 8d.

The impacts of the wave train excited by the NAT-like SSTA pattern on the summer AHS over the TP, along with its three components and associated physical variables, were examined. But how much does this influence contribute to the interannual variability of the summer AHS over the TP? Fig. 10 illustrates the explained variance (R^2) of the NAT-like SSTA pattern contributed to the summer AHS, 500-hPa vertical velocity, and 200-hPa meridional wind. In most parts of the southeastern TP region, the explained variance for the summer AHS (Fig. 10a) and 500-hPa vertical velocity (Fig. 10b) caused by the NAT-like SSTA pattern can reach 15%. Specifically, the area-averaged value of the explained variance for the summer AHS over the TP over the areas that pass the significance test shown in Fig. 8a (AHS regressed to the SST_SVD1) is approximately 20% (at the 99% confidence level). In addition, the explained variance for the 200-hPa meridional wind (Fig. 10c) generally exceeds 25%. Its spatial structure presents a wavy distribution, with the high-value centers mainly located in the NA, Norwegian Sea, eastern Europe, central Asia, India, and eastern side of the TP, consistent with the spatial distribution of the 200-hPa meridional wind anomaly shown in Fig. 4a. These findings suggest that the NAT-like SSTA pattern plays a crucial role in affecting the AHS over the TP by stimulating a teleconnection wave train on an interannual time scale in summer.

e. *Numerical simulations*

To further validate the impact of the NAT-like SSTA pattern on the interannual variability of the AHS over the TP in summer, a series of sensitivity numerical experiments were carried out utilizing the CAM6 model with SST forcing. Based on the SST_SVD1 index series obtained from Fig. 3c, a threshold of 1.0 standard deviation was applied to identify the positive and negative anomaly years related to the negative phase of the NAT-like SSTA pattern (positive anomaly years: 1987, 1991, 1998, 2010, 2012; negative anomaly years: 1992, 1994, 2000, 2002, 2013, 2015). The corresponding composite distributions of SST for these specific years are illustrated in Figs. 11a and 11b, aligning with the NAT-like SSTA pattern illustrated in Fig. 3b. For the numerical experiments, we designed two sets of experiments. The control experiment, CAM6_CTL, employed the climatological monthly SST data from the original CAM6 model. On the other hand, the sensitivity experiment, CAM6_SST, was based on the climatological monthly SST data, with the negative phase of the NAT-like SSTA pattern (depicted in Fig. 11c) obtained by subtracting the SST anomalies of negative anomaly years from those of positive anomaly years as the forcing, superimposed on the June–August period, while the SST values for the remaining months retained the climatological values. For each experiment, the CAM6 model

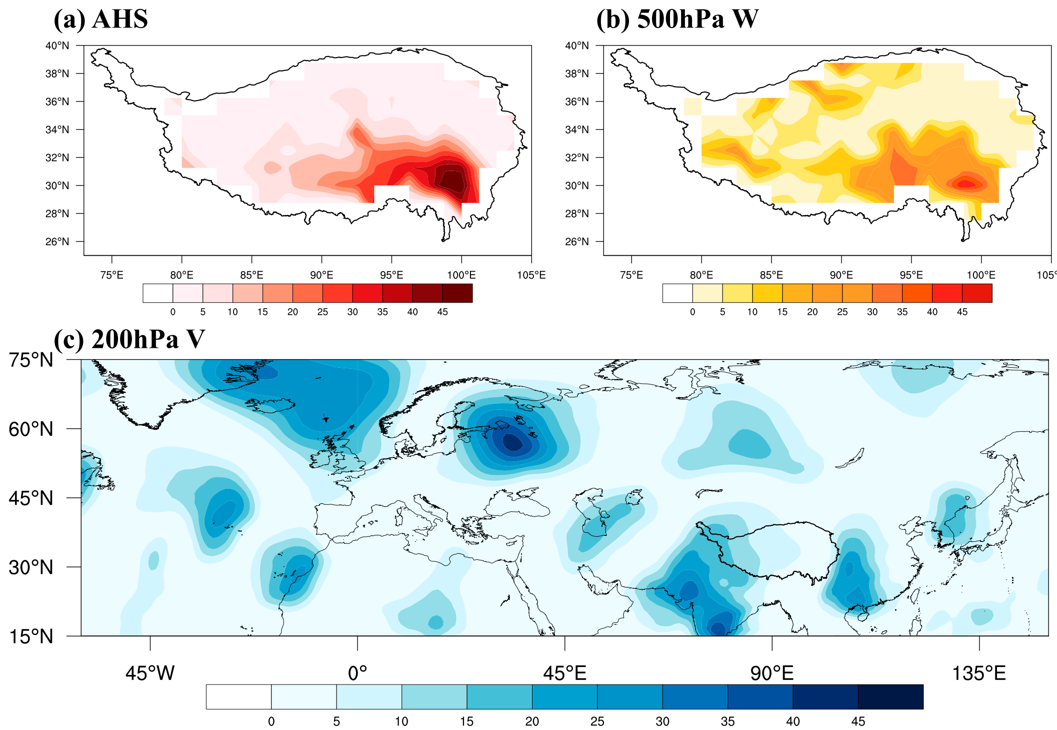

FIG. 10. The explained variance of the SST_SVD1 contributed to the summer (a) AHS, (b) 500-hPa vertical velocity (W), and (c) 200-hPa meridional wind (V) (%).

is integrated for 60 years, with the subsequent analysis focusing on the average outcomes of the last 40 years.

Figure 12 presents the difference fields of summer 200-hPa meridional wind, 500-hPa vertical velocity over the TP, the temperature, geopotential height, and vertical velocity profiles, as well as the summer AHS over the TP between the CAM6_SST experiment and the CAM6_CTL experiment, respectively. The model reproduces the influence of the NAT-like SSTA pattern on the interannual variability of the summer AHS over the TP. The results illustrate a wave train propagating from the NA across the Eurasian continent and reaching the southeastern TP (Fig. 12a), consistent with the spatial distribution of the 200-hPa meridional wind anomaly shown in Fig. 4a. Concurrently, the temperature and geopotential height fields also clearly present the propagation of the wave train (Fig. 12c), and anomalous ascending motion occurs over the TP (Fig. 12b), corresponding to the positive summer AHS anomaly (Fig. 12d). In summary, both observational

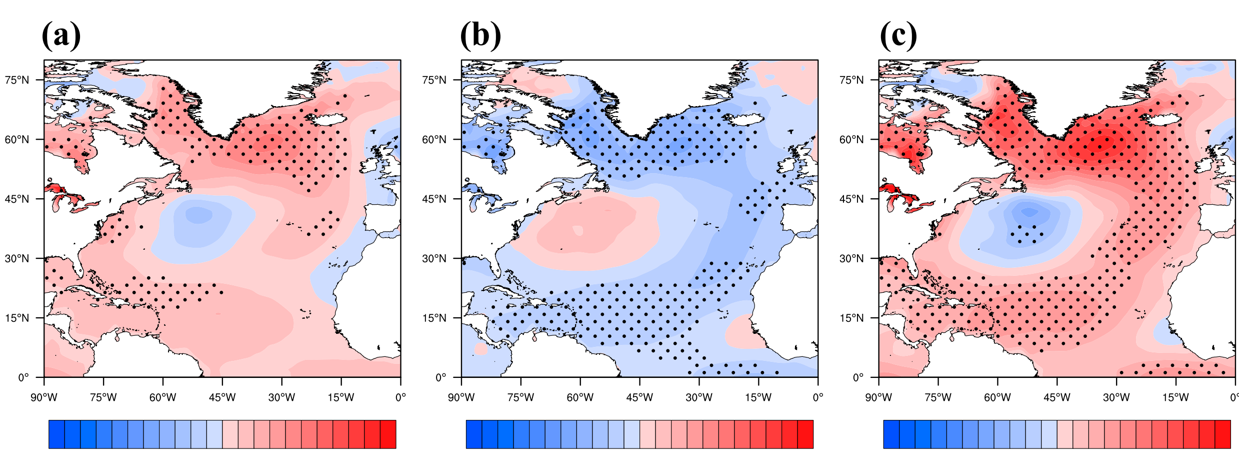

FIG. 11. The composite distributions of the summer NA SST during the (a) positive anomaly years (SST_SVD1 index greater than 1.0 standard deviation), (b) negative anomaly years (SST_SVD1 index less than −1.0 standard deviation), and (c) the differences between (a) and (b) (°C; color). The dotted areas are significant at the 90% confidence level.

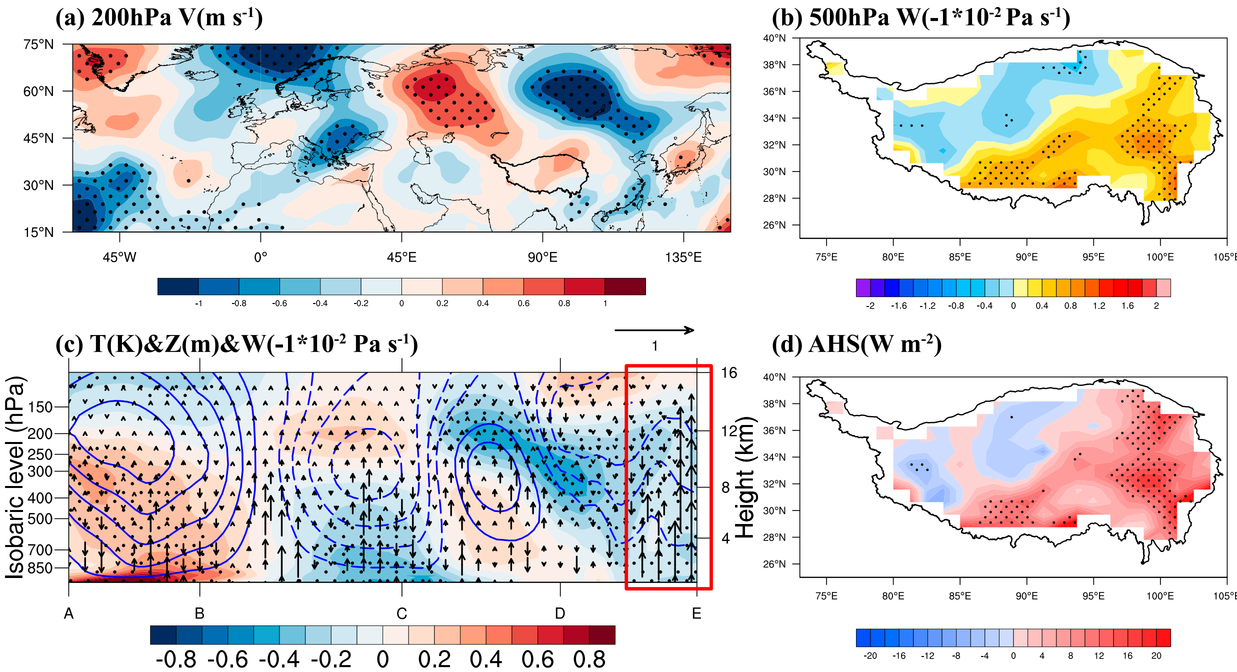

FIG. 12. The difference fields of (a) 200-hPa meridional wind (V, m s^{-1}; shading), (b) 500-hPa vertical velocity (W, -1×10^{-2} Pa s^{-1}; shading), (c) vertical cross section of temperature (T, K; shading), geopotential height (Z, m; contour), and vertical velocity (W, -1×10^{-2} Pa s^{-1}; vector) along the thick solid lines labeled A, B, C, D, and E in Fig. 4b, and (d) AHS (W m^{-2}; shading) between CAM6_SST and CAM6_CTL. The dotted areas are significant at the 90% confidence level.

data analysis and the CAM6 sensitivity experiment results indicate that the summer NAT-like SSAT pattern could trigger the teleconnection wave train across the Eurasian continent, affecting the summer AHS over the TP.

4. Conclusions and discussion

The TP, due to its distinctive topography and high altitude, acts as a powerful AHS in summer, exerting influence on both regional and global atmospheric circulation and climate. The studies available on the anomalous causes of the summer AHS over the TP mostly focus on low-latitude tropical regions, while the research on the forcing signals in mid- and high latitudes is still relatively scarce. Previous studies have shown that NA SSTA, serving as an upstream signal in mid- and high latitudes, can affect the TP thermal conditions by stimulating atmospheric teleconnection wave trains. However, current research on the impact of NA SSTA on the AHS over the TP is mostly concentrated on the winter and spring seasons. The influence of NA SSTA on the summer AHS over the TP and its underlying mechanisms and contributions remains inadequately understood. This study explores the interannual variability of the summer AHS over the TP and its relationship with concurrent NA SSTA.

The findings of the SVD analysis indicate that the NAT-like SSTA pattern significantly contributes to the interannual variability of the summer AHS over the TP. Examination of the associated circulation field reveals that the NAT-like SSTA pattern can trigger a teleconnection wave train, propagating from west to east along a great circle path, reaching the southeastern TP and inducing anomalous circulation over the TP. Subsequently, an analysis of the generation and maintenance mechanisms of this wave train is conducted. The budget analysis of the linearized vorticity equation shows a significant RWS in the western NA, and the vorticity stretching term caused by anomalous convergence and divergence plays a major role in RWS. Moreover, the zonal perturbed vorticity advection by the climatological rotating wind can be compensated by the meridional mean vorticity advection by the perturbed rotating wind, indicating that this wave train is a quasi-stationary Rossby wave. Energy balance analysis demonstrates that the contribution of the CP outweighs that of CK, suggesting that the wave train can extract available potential energy from the basic flow and is sustained through the process of baroclinic energy conversion.

Furthermore, a detailed analysis of the specific impact of the NAT-like SSTA pattern on the AHS over the TP in summer is provided. When the NAT-like SSTA pattern is in the negative phase, a positive AHS anomaly emerges over most parts of the TP, primarily driven by the latent heat released by increased precipitation. The explained variance of the NAT-like SSTA pattern contributed to the summer AHS over the southeastern TP can reach approximately 20% (at the 99% confidence level). In terms of the components of the AHS, there is an anomalous vertical upward motion associated with the wave train over the southeastern TP, promoting convection development and increasing total cloud cover. Additionally, a convergence belt of water vapor forms over the southeastern TP transporting more water vapor from the tropical oceans to this region, favoring precipitation and consequently enhancing the condensation latent heat. Concurrently, the increased precipitation reduces the T_s, diminishing $T_s - T_a$, which leads to a decrease in sensible heat. The atmospheric net radiation shows an insignificant variation due to the offsetting effects of the negative net longwave flux anomaly and the positive net shortwave flux anomaly. Finally, sensitivity experiments conducted with the CAM6 confirm that the NAT-like SSTA pattern can stimulate the teleconnection wave train that propagates downstream, affecting the summer AHS over the TP.

In this study, the focus was on exploring the connection between the summer AHS over the TP and concurrent NA SSTA. However, previous studies have shown that the NAT SSTA pattern is closely coupled with the NA Oscillation (NAO), and there is a complex interaction between the two. On the one hand, the NAO-related atmospheric circulation anomalies contribute to the NAT SSTA by modulating surface heat fluxes and the upper-ocean current. On the other hand, the NAT SSTA, in turn, could induce the NAO-related atmospheric circulation anomalies as a positive feedback through the wave-mean flow interaction and associated eddy feedback process (Czaja and Frankignoul 2002; Peng et al. 2003; Pan 2005; Hu and Huang 2006; Chen et al. 2020). The existing research indicates that the summer NAO can also affect the AHS over the TP by exciting teleconnection wave trains. When the summer NAO is in positive phase, the precipitation and AHS over the southeastern TP exhibit negative anomalies (Wang et al. 2018; Duan and Zhang 2022). Therefore, exploring the complex impacts of the summer NAO, NAT SSTA, and their interactions on the AHS over the TP is also an important aspect of our subsequent research.

In addition, previous studies have shown that the AHS over the TP is influenced by various ocean–atmosphere forcing signals originating from both mid–high latitudes and tropical regions. These signals encompass the westerly jet (Fan et al. 2018; Nan et al. 2024), atmospheric teleconnection wave trains (Han et al. 2021; Zhang and Duan 2023), ENSO (Wang and Xu 2018; Hu et al. 2021), and SSTA in the Indian and Pacific Oceans (Ji et al. 2018; Sun et al. 2021; Liu et al. 2022), etc. The interactions between NA SSTA and these signals, as well as their synergistic effects on the summer AHS over the TP, still require further investigation. On the other hand, as many scholars have pointed out, the TP plays a bridging role in the global climate teleconnections (Ma et al. 2022; Liu et al. 2024). For example, the AHS over the TP not only can respond strongly to El Niño events, Yu et al. (2022) found through observational analysis and numerical experiments that the dipole mode of surface wind speed or surface sensible heating could also be a trigger for subsequent winter El Niño events. The "negative sensible heat baroclinic structure" over the western TP in spring is modulated by the preceding NAT SSTA (Yu et al. 2021), and this mode can induce the surface westerly wind anomalies over the tropical western Pacific in May through triggering Rossby waves and modulated tropical atmospheric circulation, favoring the occurrence of subsequent El Niño events. The summer AHS over the TP, recognized as an important negative vorticity source in the midlatitude of the Northern Hemisphere (Liu et al. 2001), may also trigger teleconnection wave trains that affect the circulation and climate of downstream regions through energy propagation and dispersion effects (Wang et al. 2008; Li et al. 2021; Sun et al. 2021). Consequently, whether the summer AHS over the TP can act as a bridge and, in turn, affect the NA SSTA is also a vital scientific question worth exploring. Additionally, given the persistent nature of SSTA across seasons, it is crucial to examine whether the summer NA SSTA is a continuation of signals from the preceding winter and spring. It is also important to investigate whether the NA SSTA during winter–spring has a predictive effect on the summer AHS over the TP, which would enhance seasonal forecasting accuracy in this region.

Acknowledgments. This work was jointly supported by the National Natural Science Foundation of China (U2442207, 42122034, 42075043, and 42330609), the Youth Innovation Promotion Association (2021427), and the West Light Foundation (xbzg-zdsys-202409) of the Chinese Academy of Sciences, Key Talent Projects in Gansu Province, and the Central Guidance Fund for Local Science and Technology Development Projects in Gansu Province (24ZYQA031).

Data availability statement. 1) The monthly JRA-55 reanalysis datasets provided by the JMA are available at https://rda.ucar.edu/datasets/ds628.1/dataaccess/. 2) The monthly reanalysis datasets provided by the NCEP/NCAR can be available at https://psl.noaa.gov/data/gridded/data.ncep.reanalysis.derived.html. 3) The monthly mean SST data from the NOAA-ERSST.v5 are obtained at https://psl.noaa.gov/data/gridded/data.noaa.ersst.v5.html. 4) The monthly mean precipitation data from CRU TS4.06 are available at https://www.cru.uea.ac.uk/data. 5) The dataset of the TP boundary provided by the National Tibetan Plateau/Third Pole Environment Data Center is available at https://data.tpdc.ac.cn. 6) The datasets generated of CAM6 are available from the corresponding author on reasonable request.

REFERENCES

Chen, S., R. Wu, and W. Chen, 2020: Strengthened connection between springtime North Atlantic Oscillation and North Atlantic tripole SST pattern since the late 1980s. *J. Climate*, **33**, 2007–2022, https://doi.org/10.1175/JCLI-D-19-0628.1.

Cheng, S., and Coauthors, 2024: Impact of summer North Atlantic sea surface temperature tripole on precipitation over mid-high-latitude Eurasia. *J. Climate*, **37**, 5037–5053, https://doi.org/10.1175/JCLI-D-24-0072.1.

Cui, Y., A. Duan, Y. Liu, and G. Wu, 2015: Interannual variability of the spring atmospheric heat source over the Tibetan Plateau forced by the North Atlantic SSTA. *Climate Dyn.*, **45**, 1617–1634, https://doi.org/10.1007/s00382-014-2417-9.

Czaja, A., and C. Frankignoul, 2002: Observed impact of Atlantic SST anomalies on the North Atlantic oscillation. *J. Climate*, **15**, 606–623, https://doi.org/10.1175/1520-0442(2002)015<0606:OIOASA>2.0.CO;2.

Danabasoglu, G., and Coauthors, 2020: The Community Earth System Model version 2 (CESM2). *J. Adv. Model. Earth Syst.*, **12**, e2019MS001916, https://doi.org/10.1029/2019MS001916.

Dong, W., Y. Lin, J. S. Wright, Y. Xie, F. Xu, W. Xu, and Y. Wang, 2017: Indian monsoon low-pressure systems feed up-and-over moisture transport to the southwestern Tibetan Plateau. *J. Geophys. Res. Atmos.*, **122**, 12 140–12 151, https://doi.org/10.1002/2017JD027296.

Duan, A., and P. Zhang, 2022: Interannual variability of atmospheric heat source over the Tibetan Plateau and its driving factors (in Chinese). *Chin. J. Atmos. Sci.*, **46**, 455–472, https://doi.org/10.3878/j.issn.1006-9895.2201.21126.

Fan, W., W. Ma, Y. Zheng, and Z. Yang, 2018: Long-term variation of surface heating over the Qinghai-Tibetan Plateau linked to the westerly jet (in Chinese). *Plateau Meteor.*, **37**, 591–601.

Fang, J., and X.-Q. Yang, 2016: Structure and dynamics of decadal anomalies in the wintertime midlatitude North Pacific ocean-atmosphere system. *Climate Dyn.*, **47**, 1989–2007, https://doi.org/10.1007/s00382-015-2946-x.

Han, S., H. Ren, B. Su, and J. Li, 2022: Connection between the North Atlantic sea surface temperature and the late autumn snow cover anomalies over the central Tibetan Plateau. *Atmos. Res.*, **279**, 106405, https://doi.org/10.1016/j.atmosres.2022.106405.

Han, Y., W. Ma, Y. Yang, Y. Ma, Z. Xie, G. Sun, M. Menenti, and B. Su, 2021: Impacts of the Silk Road pattern on the interdecadal variations of the atmospheric heat source over the Tibetan Plateau. *Atmos. Res.*, **260**, 105696, https://doi.org/10.1016/j.atmosres.2021.105696.

Harris, I., T. J. Osborn, P. Jones, and D. Lister, 2020: Version 4 of the CRU TS monthly high-resolution gridded multivariate climate dataset. *Sci. Data*, **7**, 109, https://doi.org/10.1038/s41597-020-0453-3.

Hu, J., and A. Duan, 2015: Relative contributions of the Tibetan Plateau thermal forcing and the Indian Ocean Sea surface temperature basin mode to the interannual variability of the East Asian summer monsoon. *Climate Dyn.*, **45**, 2697–2711, https://doi.org/10.1007/s00382-015-2503-7.

Hu, S., T. Zhou, and B. Wu, 2021: Impact of developing ENSO on Tibetan Plateau summer rainfall. *J. Climate*, **34**, 3385–3400, https://doi.org/10.1175/JCLI-D-20-0612.1.

Hu, Z., and B. Huang, 2006: Air-sea coupling in the North Atlantic during summer. *Climate Dyn.*, **26**, 441–457, https://doi.org/10.1007/s00382-005-0094-4.

Huang, B., and Coauthors, 2017: Extended Reconstructed Sea Surface Temperature, version 5 (ERSSTv5): Upgrades, validations, and intercomparisons. *J. Climate*, **30**, 8179–8205, https://doi.org/10.1175/JCLI-D-16-0836.1.

Huang, J., and Coauthors, 2023: Global climate impacts of land-surface and atmospheric processes over the Tibetan Plateau. *Rev. Geophys.*, **61**, e2022RG000771, https://doi.org/10.1029/2022RG000771.

Ji, C., Y. Zhang, Q. Cheng, Y. Li, T. Jiang, and X. S. Liang, 2018: On the relationship between the early spring Indian Ocean's sea surface temperature (SST) and the Tibetan Plateau atmospheric heat source in summer. *Global Planet. Change*, **164**, 1–10, https://doi.org/10.1016/j.gloplacha.2018.02.011.

Jiang, X., Y. Li, S. Yang, K. Yang, and J. Chen, 2016: Interannual variation of summer atmospheric heat source over the Tibetan Plateau and the role of convection around the western Maritime Continent. *J. Climate*, **29**, 121–138, https://doi.org/10.1175/JCLI-D-15-0181.1.

Kalnay, E., and Coauthors, 1996: The NCEP/NCAR 40-Year Reanalysis Project. *Bull. Amer. Meteor. Soc.*, **77**, 437–471, https://doi.org/10.1175/1520-0477(1996)077<0437:TNYRP>2.0.CO;2.

Kobayashi, S., and Coauthors, 2015: The JRA-55 Reanalysis: General specifications and basic characteristics. *J. Meteor. Soc. Japan*, **93**, 5–48, https://doi.org/10.2151/jmsj.2015-001.

Kosaka, Y., and H. Nakamura, 2006: Structure and dynamics of the summertime Pacific-Japan teleconnection pattern. *Quart. J. Roy. Meteor. Soc.*, **132**, 2009–2030, https://doi.org/10.1256/qj.05.204.

Lai, H., H. W. Chen, J. Kukulies, T. Ou, and D. Chen, 2021: Regionalization of seasonal precipitation over the Tibetan Plateau and associated large-scale atmospheric systems. *J. Climate*, **34**, 2635–2651, https://doi.org/10.1175/JCLI-D-20-0521.1.

Li, Q., M. Zhao, S. Yang, X. Shen, L. Dong, and Z. Liu, 2021: A zonally-oriented teleconnection pattern induced by heating of the western Tibetan Plateau in boreal summer. *Climate Dyn.*, **57**, 2823–2842, https://doi.org/10.1007/s00382-021-05841-6.

Lin, S. J., and R. B. Rood, 1997: An explicit flux-form semi-Lagrangian shallow-water model on the sphere. *Quart. J. Roy. Meteor. Soc.*, **123**, 2477–2498, https://doi.org/10.1002/qj.49712354416.

Liu, J., X. Guan, Z. Gao, X. Huang, J. Ma, Y. He, and T. Xie, 2022: Inter-decadal variability of the heat source over the Tibetan Plateau. *Climate Dyn.*, **58**, 729–739, https://doi.org/10.1007/s00382-021-05929-z.

Liu, S., A. Duan, and G. Wu, 2020: Asymmetrical response of the East Asian summer monsoon to the quadrennial oscillation of global sea surface temperature associated with the Tibetan Plateau thermal feedback. *J. Geophys. Res. Atmos.*, **125**, e2019JD032129, https://doi.org/10.1029/2019JD032129.

Liu, X., G. Wu, W. Li, and Y. Liu, 2001: Thermal adaptation of heating and large scale flow fields on the Qinghai Tibet Plateau in summer (in Chinese). *Prog. Nat. Sci.*, **11**, 35–41.

Liu, Y., M. Lu, H. Yang, A. Duan, B. He, S. Yang, and G. Wu, 2020: Land-atmosphere-ocean coupling associated with the Tibetan Plateau and its climate impacts. *Natl. Sci. Rev.*, **7**, 534–552, https://doi.org/10.1093/nsr/nwaa011.

——, W. Yu, J. Jiang, T. Ma, J. Mao, and G. Wu, 2024: The Tibetan Plateau bridge: Influence of remote teleconnections from extratropical and tropical forcings on climate anomalies. *Atmos. Ocean. Sci. Lett.*, **17**, 100396, https://doi.org/10.1016/j.aosl.2023.100396.

Luo, H., and Coauthors, 2024: Impact of the summer atmospheric heat source over the Tibetan Plateau on interannual variability of meridional circulation on the north side of the Tibetan Plateau. *J. Climate*, **37**, 3543–3561, https://doi.org/10.1175/JCLI-D-23-0599.1.

Ma, T., G. Wu, Y. Liu, and J. Mao, 2022: Abnormal warm sea-surface temperature in the Indian Ocean, active potential vorticity over the Tibetan Plateau, and severe flooding along the Yangtze River in summer 2020. *Quart. J. Roy. Meteor. Soc.*, **148**, 1001–1019, https://doi.org/10.1002/qj.4243.

Nan, S., G. Liu, Y. Bao, and D. Chen, 2024: Link between the atmospheric thermal condition over the Tibetan-Iranian Plateaus and Eurasian-African climate through the Asian westerly jet stream. *Theor. Appl. Climatol.*, **155**, 2427–2438, https://doi.org/10.1007/s00704-024-04828-7.

Pan, L., 2005: Observed positive feedback between the NAO and the North Atlantic SSTA tripole. *Geophys. Res. Lett.*, **32**, L06707, https://doi.org/10.1029/2005GL022427.

Peng, S., W. Robinson, and S. Li, 2003: Mechanisms for the NAO responses to the North Atlantic SST tripole. *J. Climate*, **16**, 1987–2004, https://doi.org/10.1175/1520-0442(2003)016<1987:MFTNRT>2.0.CO;2.

Sardeshmukh, P. D., and B. J. Hoskins, 1988: The generation of global rotational flow by steady idealized tropical divergence. *J. Atmos. Sci.*, **45**, 1228–1251, https://doi.org/10.1175/1520-0469(1988)045<1228:TGOGRF>2.0.CO;2.

Sun, B., and H. Wang, 2019: Enhanced connections between summer precipitation over the Three-River-Source region of China and the global climate system. *Climate Dyn.*, **52**, 3471–3488, https://doi.org/10.1007/s00382-018-4326-9.

Sun, X., Y. Ding, and Q. Li, 2021: Interdecadal variation of the atmospheric heat source over the Tibetan Plateau and surrounding Asian monsoon region: Impact on the Northern Hemisphere summer circulation. *J. Meteor. Res.*, **35**, 238–257, https://doi.org/10.1007/s13351-021-0101-7.

Takaya, K., and H. Nakamura, 2001: A formulation of a phase-independent wave-activity flux for stationary and migratory quasigeostrophic eddies on a zonally varying basic flow. *J. Atmos. Sci.*, **58**, 608–627, https://doi.org/10.1175/1520-0469(2001)058<0608:AFOAPI>2.0.CO;2.

Wang, C., and Z. Ma, 2018: Quasi-3-yr cycle of rainy season precipitation in Tibet related to different types of ENSO during 1981–2015. *J. Meteor. Res.*, **32**, 181–190, https://doi.org/10.1007/s13351-018-7100-3.

Wang, Y., and X. Xu, 2018: Impact of ENSO on the thermal condition over the Tibetan Plateau. *J. Meteor. Soc. Japan*, **96**, 269–281, https://doi.org/10.2151/jmsj.2018-032.

——, B. Zhang, L. Chen, J. He, W. Li, and H. Chen, 2008: Relationship between the atmospheric heat source over Tibetan Plateau and the heat source and general circulation over East Asia. *Chin. Sci. Bull.*, **53**, 3387–3394, https://doi.org/10.1007/s11434-008-0327-0.

Wang, Z., S. Yang, N. Lau, and A. Duan, 2018: Teleconnection between summer NAO and East China rainfall variations: A bridge effect of the Tibetan Plateau. *J. Climate*, **31**, 6433–6444, https://doi.org/10.1175/JCLI-D-17-0413.1.

——, ——, H. Luo, and J. Li, 2022: Drying tendency over the southern slope of the Tibetan Plateau in recent decades: Role of a CGT-like atmospheric change. *Climate Dyn.*, **59**, 2801–2813, https://doi.org/10.1007/s00382-022-06262-9.

Wu, G., W. Li, H. Guo, H. Liu, J. Xue, and Z. Wang, 1997: Sensible heat driven air-pump over the Tibetan Plateau and its impacts on the Asian summer monsoon. *Collections on the Memory of Zhao Jiuzhang*, D. Ye, Ed., Chinese Science Press, 116–126.

——, Y. Liu, B. Dong, X. Liang, A. Duan, Q. Bao, and J. Yu, 2012: Revisiting Asian monsoon formation and change associated with Tibetan Plateau forcing: I. Formation. *Climate Dyn.*, **39**, 1169–1181, https://doi.org/10.1007/s00382-012-1334-z.

——, ——, B. He, Q. Bao, and Z. Wang, 2018: Review of the impact of the Tibetan Plateau sensible heat driven air-pump on the Asian summer monsoon (in Chinese). *Chin. J. Atmos. Sci.*, **42**, 488–504, https://doi.org/10.3878/j.issn.1006-9895.1801.17279.

Wu, Z., B. Wang, J. Li, and F. Jin, 2009: An empirical seasonal prediction model of the East Asian summer monsoon using ENSO and NAO. *J. Geophys. Res.*, **114**, D18120, https://doi.org/10.1029/2009JD011733.

Xie, Y., and Coauthors, 2023: Oceanic repeaters boost the global climatic impact of the Tibetan Plateau. *Sci. Bull.*, **68**, 2225–2235, https://doi.org/10.1016/j.scib.2023.07.019.

Xu, P., L. Wang, and W. Chen, 2019: The British-Baikal Corridor: A teleconnection pattern along the summertime polar front jet over Eurasia. *J. Climate*, **32**, 877–896, https://doi.org/10.1175/JCLI-D-18-0343.1.

——, ——, and Z. Dong, 2022: The British-Okhotsk Corridor pattern and its linkage to the Silk Road pattern. *J. Climate*, **35**, 5787–5804, https://doi.org/10.1175/JCLI-D-21-0705.1.

Yang, K., J. Qin, X. Guo, D. Zhou, and Y. Ma, 2009: Method development for estimating sensible heat flux over the Tibetan Plateau from CMA data. *J. Appl. Meteor. Climatol.*, **48**, 2474–2486, https://doi.org/10.1175/2009JAMC2167.1.

——, H. Wu, J. Qin, C. Lin, W. Tang, and Y. Chen, 2014: Recent climate changes over the Tibetan Plateau and their impacts on energy and water cycle: A review. *Global Planet. Change*, **112**, 79–91, https://doi.org/10.1016/j.gloplacha.2013.12.001.

Ye, D., and Y. Gao, 1979: *Meteorology of the Qinghai-Xizang Plateau*. Science Press, 278 pp.

Yu, J., Y. Liu, and G. Wu, 2011: An analysis of the diabatic heating characteristic of atmosphere over the Tibetan Plateau in winter I: Climatology. *Acta Meteor. Sin.*, **69**, 79–88, https://doi.org/10.11676/qxxb2011.007.

Yu, W., Y. Liu, X. Yang, G. Wu, B. He, J. Li, and Q. Bao, 2021: Impact of North Atlantic SST and Tibetan Plateau forcing on seasonal transition of springtime South Asian monsoon circulation. *Climate Dyn.*, **56**, 559–579, https://doi.org/10.1007/s00382-020-05491-0.

——, ——, L. Xu, G. Wu, S. Yang, and D. Chen, 2022: Potential impact of spring thermal forcing over the Tibetan Plateau on the following winter El Niño-Southern Oscillation. *Geophys. Res. Lett.*, **49**, e2021GL097234, https://doi.org/10.1029/2021GL097234.

——, and Coauthors, 2023: Potential impact of winter–spring North Atlantic tripole SSTAs on the following autumn–winter El Niño–Southern Oscillation: Bridging role of the Tibetan Plateau. *Geophys. Res. Lett.*, **50**, e2022GL100663, https://doi.org/10.1029/2022GL100663.

Zhang, P., and A. Duan, 2023: Precipitation anomaly over the Tibetan Plateau affected by tropical sea-surface temperatures and mid-latitude atmospheric circulation in September (in Chinese). *Sci. China Earth Sci.*, **66**, 619–632, https://doi.org/10.1007/s11430-022-1067-8.

——, ——, and J. Hu, 2022: Combined effect of the tropical Indian Ocean and tropical North Atlantic sea surface temperature anomaly on the Tibetan Plateau precipitation anomaly in late summer. *J. Climate*, **35**, 7499–7518, https://doi.org/10.1175/JCLI-D-21-0990.1.

Zhang, Y., B. Li, and D. Zheng, 2014: Publication of data in the paper “On the Scope and Area of the Tibetan Plateau”: GIS data of Tibetan Plateau boundary and area (in Chinese). *Acta Geogr. Sin.*, **69**, 65–68.

Zhao, Y., and T. Zhou, 2021: Interannual variability of precipitation recycle ratio over the Tibetan Plateau. *J. Geophys. Res. Atmos.*, **126**, e2020JD033733, https://doi.org/10.1029/2020JD033733.

——, A. Duan, and G. Wu, 2018: Interannual variability of late-spring circulation and diabatic heating over the Tibetan Plateau associated with Indian Ocean forcing. *Adv. Atmos. Sci.*, **35**, 927–941, https://doi.org/10.1007/s00376-018-7217-4.

Zhou, C., P. Zhao, and J. Chen, 2019: The interdecadal change of summer water vapor over the Tibetan Plateau and associated mechanisms. *J. Climate*, **32**, 4103–4119, https://doi.org/10.1175/JCLI-D-18-0364.1.

Zuo, J., W. Li, C. Sun, L. Xu, and H. Ren, 2013: Impact of the North Atlantic sea surface temperature tripole on the East Asian summer monsoon. *Adv. Atmos. Sci.*, **30**, 1173–1186, https://doi.org/10.1007/s00376-012-2125-5.